

Accessing slip activity in high purity tin with electron backscatter diffraction and measurement of slip strength

Tianhong Gu*, Finn Giuliani, and T. Ben Britton

Department of Materials, Imperial College London, SW7 2AZ. UK

*Corresponding author: t.gu15@imperial.ac.uk

Abstract

β -tin has been used widely as an interconnect in modern electronics. To improve the understanding of the reliability of these components, we directly measure the critical resolved shear stress of individual slip systems in β -tin using micropillar compression tests at room temperature with crystal orientations near-[100] and [001] in the loading direction within a large grain high purity tin (99.99%) sample. This activates the (110)[$\bar{1}11$]/2, ($1\bar{1}0$)[$\bar{1}\bar{1}1$]/2, (010)[001] and (110)[001] slip systems. Analysis of the slip traces and load-displacement curves enables measurement of the critical resolved shear stress for $\dot{\epsilon} = 10^{-4}$ of

$$\tau_{CRSS}^{\{110\}\langle\bar{1}11\rangle/2} = 10.4 \pm 0.4 \text{ and } \tau_{CRSS}^{\{010\}\langle 001\rangle} = 3.9 \pm 0.3 \text{ MPa.}$$

Keywords: Pb-free solder, Tin, Micromechanics, Dislocation slip and FIB.

As demand for multifunction and high-performance devices increases, there is a need to consider device miniaturisation for wider applications in electronic interconnections. With the development of fine pitch structures in electronic devices and components, the assembly density has become higher, the solder joints have become smaller in size. This leads to greater electrical, thermal and mechanical loads to be carried by the solder joints and resulting issues in long-term integrity and reliability of electronic interconnections ^[1-4]. Furthermore, due to the environment and health concerns on lead (Pb) ^[5], Pb-free solders have been replacing the traditional Sn-37Pb solders in electronic interconnections. For example, in electronic devices, such as mobile phones and computers. These Pb-free solders are tin (Sn) based alloys. Their main phase is β -Sn, which has a body centred tetragonal structure with a shorter c-axis ^[6, 7], this results in anisotropic thermomechanical properties ^[8, 9]. Therefore, it is very important to understand the mechanical behaviour and deformation mechanisms of Sn, which requires us to have single crystal measurements to determine the slip systems for a particular orientation.

There has been significant amount of work on the mechanical behaviour of either entire solder joints ^[10-16] or large bulk samples ^[17-21]. Among them, Matin et al. ^[19, 22], Zamiri et al. ^[23], Zhou et al. ^[24], Bieler et al. ^[10] and Zou et al. ^[25] have attempted to measure (experimentally) the critical resolved shear stress (τ_{CRSS}) values of β -Sn. (The CRSS ratios are given in Supplementary Table S1). However, these measurements have been extracted from bulk samples containing both intermetallics and β -Sn phases. Zamiri et al. ^[23], Zhou et al. ^[24], Bieler et al. ^[10] and Zou et al. ^[25] have considered different crystal orientations for single-crystal Sn-3.0Ag-0.5Cu solder joints under uniaxial tensile test at a strain rate of $3 \times 10^{-6} \text{ s}^{-1}$ and room temperature from Zhou et al. ^[24], who considered a range of phases (e.g. Cu_6Sn_5 , Ag_3Sn and β -Sn) as a whole. Similarly, the τ_{CRSS} values used by Matin et al. ^[19, 22] were extracted from

polycrystal Sn-3.8Ag-0.7Cu solder dog-bone samples by Matin et al. [19] at a constant strain rate and 293 K.

Previously, Mayer et al [26] and Gu et al. [20, 21] have demonstrated the change in mechanical behaviour in the dendritic and eutectic regions by performing micropillar compression for Sn-3.5Ag solder alloy (μm scale) [26] and tensile creep tests for Sn-3.0Ag-0.5Cu solder alloy (mm scale) [20, 21] by separating the intermetallics-containing eutectic region and intermetallics-free dendritic β -Sn region. However, no direct measurements of τ_{CRSS} have been carried out for their works [20, 21, 26]. Therefore, there is a need to remove these uncertainties such as crystal orientations, number of grains and different phases (e.g. β -Sn Cu_6Sn_5 and Ag_3Sn) from the previously used τ_{CRSS} values and to obtain precise values of τ_{CRSS} by isolating the β -Sn phase from the bulk.

Micropillar compression testing has been used to investigate the micromechanics of an individual microstructural unit for many materials in smaller lengthscale [27-29], at specific crystal orientations [26, 30-33] enabling the understanding of the mechanical property such as τ_{CRSS} of the material [34, 35]. In solder samples, a few studies have focussed on extracting properties of the intermetallics [26, 33, 36] but these did not isolate the soft β -Sn phase.

For the β -Sn phase, deformation can occur within a grain [26, 37] or at a grain boundary [38, 39]. Prior work has explored grain boundary deformation (noting that β -Sn is hot at room temperature and likely has significant grain boundary sliding). Gong et al. [39] showed a size dependence for grain boundary sliding in β -Sn, reported that the resistance of grain boundary sliding increases as pillar size decreases from 5 to 1 μm in width (mid-height). For these grain boundary sliding experiments, the micropillars have their a-axes about 18° and 26° towards the loading axis and compressed with displacement rate of 2 and 20 nm/s. During their tests, Gong et al. [39] observed occurrence of multiple slips but without determining the activated slip

systems. Additionally, Kaira et al. [38] focused on evaluation of grain boundary effect on deformation mechanisms of pure tin, where circular micropillar tests were carried out at a strain rate of $\sim 10^{-3} \text{ s}^{-1}$ with dimensions of $2 \times 6 \text{ }\mu\text{m}$. Kaira et al. [38] found out that the pillars with a $\{301\}$ twin boundary has early yielding behaviour and more strain bursts than the single-crystalline micropillars. Kaira et al. [38] selected the crystal orientations at random, compressing along $(33 \bar{1}3 25)$, $(\bar{1}9 20 11)$ and $(\bar{5} \bar{2} 4)$ and observed activation of slip systems $(001)[100]$, $(100)[001]$ and $(110)[\bar{1}11]/2$ respectively both in single crystal and the bi-crystal sample [38], and for these tests no τ_{CRSS} values were reported.

Single crystal testing was performed by Philippi et al. [37], who tested pillars along $[001]$ and $[110]$ in the SEM and using in-situ testing with observations using micro-Laue X-ray diffraction. Both pillars deformed with multiple slip systems activating, as evidenced by slip traces on the side of the pillars and they found a size effect for pillars tested below $10 \text{ }\mu\text{m}$ in width (pillars had an aspect ratio of 3 length to 1 width). Their tests showed that that the $[001]$ orientated pillar has a higher the flow stress than the $[110]$ orientated pillar, by a factor of ~ 1.3 , and the size effect term was similar between both pillars [37].

For the present work, we extend on the prior studies by performing our micropillar compression tests on directionally solidified high purity tin (HP Sn) samples (99.99%) by considering the β -Sn phase only and directly selecting grains that activate limited system activity, which results in at most two slip systems operating. Analysis of the slip traces and combining this with the load-displacement curves enables us to extract the τ_{CRSS} values for each slip system and to calibrate the ranking of the slip systems [40] and measure the relative slip strengths of the β -tin system at room temperature ($\frac{T}{T_m} = 0.6$ [41]). This work should enable future work to calibrate crystal plasticity-based models of solder materials.

A large bulk high purity tin (HP Sn) sample containing ~99.99% β -Sn phase was used for micropillar fabrication, in order to focus on the properties of β -Sn phase only and avoid the influence from eutectic structure and any inclusion. The sample was directionally solidified by Bridgman growth at pulling rate of $v = 20 \mu\text{m/s}$ to not only remove damages from pre-deformation but also produce a controlled single crystal orientation (Near-[100] in *Figure 1a*), which has a 23° deviation angle from its $\langle 100 \rangle$ to the loading direction (*Table 1*). The second orientation (Near-[001] in *Figure 1a*) has a 22° deviation angle from its $\langle 001 \rangle$ to the loading direction (*Table 1*) was formed by cutting at the edge of the sample and propagated across the sample. The misorientation of the two grains within the scanned region is less than 2° (*Figure 1d*). The corresponding pole figure (PF) shows that the two grains share a common $\{100\}$ plane and are separated by approx. 63° , which means the near-[001] grain is the mechanical deformation twin grain of the near-[100] grain (*Figure 1b*) (we took the advantage of a mechanical twin to access the two orientations). These two grains were selected because of the large anisotropic behaviour between the $\langle 100 \rangle$ and $\langle 001 \rangle$ of β -Sn^[6, 7]. The crystal orientation of the sample was characterised using electron backscatter diffraction (EBSD) with a step size of $4 \mu\text{m}$ and its cross-sectional surface was revealed by polishing with a colloidal silica and the quality of the final surface was improved using a broad ion beam milling (Gatan PECS II).

An array of the micropillars (*Figure 1c*) was cut within the two grains by Ga FIB using a FEI Helios Nanolab 600 Dual beam microscope at an accelerating voltage of 30 kV and with reducing ion beam current from 9 nA to 280 pA (as set up in *Figure 1d*) into rectangular shapes with dimension of $5 \times 5 \mu\text{m}$ in width at mid-height and $\sim 13 \mu\text{m}$ in height to achieve an aspect ratio (width/length) of 1:2.6 (*Figure 1e & f*). The calculated taper angle of the micropillars is $\sim 2^\circ$. A script was set up using Thermo Scientific NanoBuilder software for the FIB milling.

The in-situ micropillar compression tests were performed using a displacement-controlled Alemnis nanoindentation stage at room temperature inside a Quanta FEG 450 SEM as set up in *Figure 1g*. High resolution displacement control is helpful in near uniaxial micropillar testing where load control can be inherently unstable and (near) unconstrained slip in a micropillar, which can result in artifacts as the slip bands form and shear the pillar either side of the slip plane.

A 10 μm diameter circular flat punch indenter was used to achieve a uniaxial stress state for the compression test. The pillars were deformed with a displacement of ~ 0.13 , 0.65 and 1.3 μm , which gives 1, 5 and 10% of engineering strain. The applied loading and unloading speed were 0.01 and 0.1 $\mu\text{m/s}$ respectively, which results in a strain rate of $7.7 \times 10^{-4} \text{ s}^{-1}$ during compression.

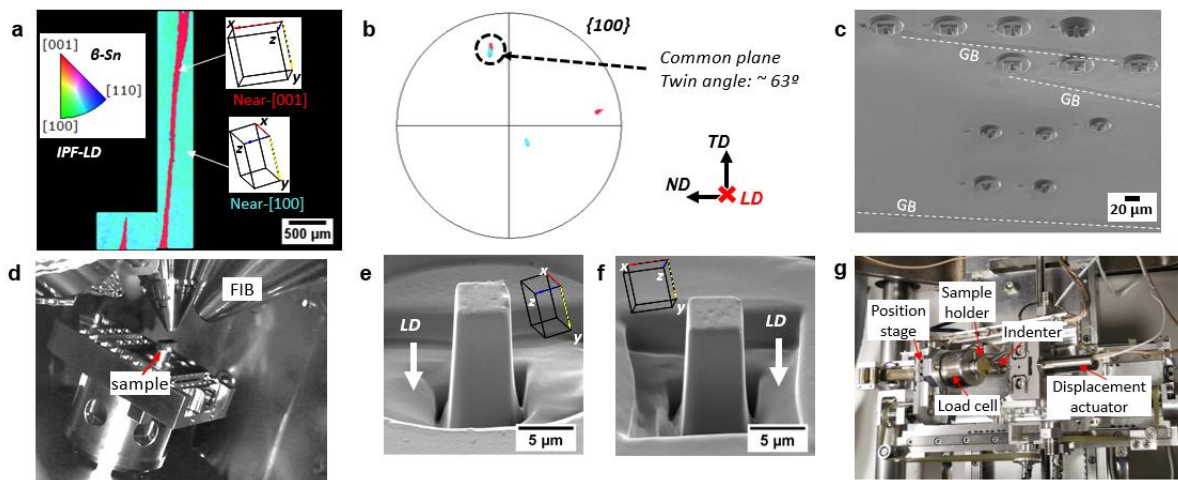


Figure 1. (a) IPF-LD (Crystal orientations represented with EBSD inverse pole figure colouring with respect to the loading direction, IPFZ) map of HP Sn sample after directional solidification (DS) with crystal unit cells inserted representing the tested crystal orientations. (b) Pole figure (PF) of the sample after DS. (c) Secondary electron (SE) image showing the arrays of micropillars with grain boundaries labelled. (d) FIB set-up in SEM. (e, f) SE images of pre-deformed micropillars for (e) near-[100] and (f) near-[001] orientations. (g) Alemnis nanoindentation stage for in-situ compression test.

Figure 2b and d show the engineering stress-strain curves for compression test of the two sets of differently orientated micropillars (Table 1). The near-[100] micropillar (Figure 2a & b) has a higher average yield stress, σ_y than the near-[001] pillar (Table 1). The average flow stress for the near-[100] pillar is about two times higher than the near-[001] pillar (Table 1). The σ_y is determined by differentiating the engineering stress (σ_y) with respect to engineering strain (ϵ). The $\frac{d\sigma}{d\epsilon}$ vs. ϵ curves in supplementary Figure S2 reach a linear relationship with a constant gradient close to 0 once the yield point is achieved. For both pillars, the flow stress (σ_f), increases constantly from the yield point up to the applied 1, 5 and 10% strain and they exhibit significant strain hardening showing as a general increase in the stress with increasing strain (Figure 2b & d) and strengthening the micropillars.

Figure 2e - l contains the micrographs for the pillars after compression (10% strain). Shape distortions are observed for both the near-[100] and near-[001] orientated pillars by comparing the pre-deformed images (Figure 1e & f) with the full-viewed post-deformed images (Figure 2e - l). The dashed lines overlaid on the micrographs show the trend of observed slip traces. For the near-[100] pillar, two sets of slip traces appear on each side surface from the top corner to the side edge indicated with red dashed lines and between side edges indicated with blue dashed lines (Figure 2e - h), implying the activation of two different slip systems. Similarly, two obvious slip traces resulted from two activated slip systems are observed on each side surface of the near-[001] pillar after compression (Figure 2i - l). The slip traces appear from the top corner to the bottom and between the side edges indicated with blue and red dashed lines accordingly in Figure 2i - l. Noticeably, the pillars form multiple closely spaced slip traces during deformation indicated with red and blue arrows in Figure 2e - l. As shown in the corresponding stress-strain curves in Figure 2b and d, both of the pillars deform with two stage strain hardening (indicated with arrows in Figure 2b & d), implying that higher level of applied

stress is required to move the dislocations to continue the plastic deformation for activation of second slip system, where the initial crystal orientation rotates to prefer the second slip system. Additionally, the gradient of the loading curve is different to the corresponding unloading curves (*Figure 2b & d*) because the pillars are misaligning, i.e. rotating slightly when the punch indenter becomes into contact with the pillar and some dislocations are activated at the very early stage of deformation, implying there is the microplasticity taken place, i.e. the first slip system is activated at a much lower strain ($\langle\sigma_y$) for the pillars. Although slight deviation of each set of slip traces are observed for both of the pillars (*Figure 2e - l*), the traces are straight over a large strain range (up to 10% engineering strain), so single slip is still confirmed.

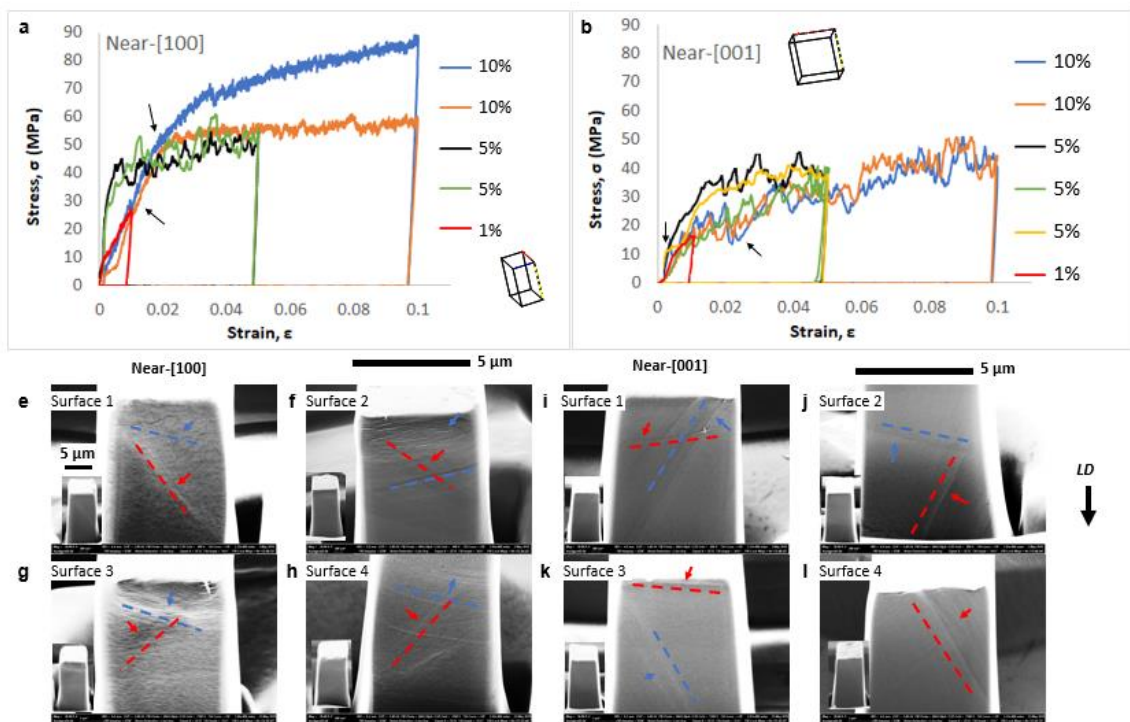


Figure 2. (b, d) Engineering stress-strain curves for micropillars of the two grains. (e - l) SE images of deformed micropillars for (e - h) near-[100] and (i - l) near-[001] orientations with two experimental slip traces highlighted using blue and red dashed lines.

The analysis of slip traces has been used to evaluate which slip system is more likely to be activated. *Table 1* demonstrates the σ_f , σ_y and τ_{CRSS} values for single slip of the tested pillars. By analysing the experimental slip traces for both near-[100] and near-[001] orientated pillars, the Schmid factor, m can be calculated for the activated slip system(s). The m values are calculated by dividing the τ_{CRSS} with the corresponding the σ_y of each activated slip system. The two τ_{CRSS} obtained at room temperature are $\tau_{CRSS}^{\{110\}\langle\bar{1}11\rangle/2} \sim 10.4 \pm 0.4$ MPa for slip system (110)[$\bar{1}11$]/2 and (1 $\bar{1}0$)[$\bar{1}\bar{1}1$]/2 and $\tau_{CRSS}^{\{010\}\langle 001\rangle} \sim 3.9 \pm 0.3$ MPa for slip system (010)[001] and (110)[001].

In other work, the weighted Schmid factor, m_W values are used to scale the relative τ_{CRSS} for the slip systems. The τ_{CRSS} values we claimed are approximately three to four times larger than the values reported by Matin et al. [19], which were estimated by correlating the slip systems with atomic line density (Peierls model based). However, our values have a good consistency with the results obtained by macroscopic tensile testing extracted from Zamiri et al. [23].

Orientation of β -Sn	Average σ_y (MPa)	STD	Average σ_f (MPa)	STD	τ_{CRSS} (MPa)	m	CRSS ratio	Activated SS
23° to $\langle 100 \rangle$	25.0	4.6	55.9	10.5	10.4 ± 0.4	0.42	1.11	(110)[$\bar{1}11$]/2 (1 $\bar{1}0$)[$\bar{1}\bar{1}1$]/2
22° to $\langle 001 \rangle$	10.9	1.4	30.0	2.6	3.9 ± 0.3	0.36	1	(010)[001] (110)[001]

Table 1. Summary of results showing the crystal orientation, average yield stress (σ_y), average flow stress (σ_f), CRSS (τ_{CRSS}), Schmid factor (m) and the activated slip system of the two pillars with standard deviation (STD) calculated from average of 5 and 7 pillars for the near-[100] and near-[001] samples respectively (see Supplementary Table S3).

The m_W can be calculated according to the critical resolved shear stress (τ_{CRSS}) and Schmid factor (m), as given in Equation (1).

$$m_W = \frac{m}{\tau_{CRSS}/\tau_{CRSS}^{[001]}} \quad (1)$$

Where $\tau_{CRSS} = \frac{F}{A} \cos\phi \cos\lambda$ and the Schmid factor, $m = \cos\phi \times \cos\lambda$.

The blue and red dashed lines shown on the models in *Figure 3a* and *Figure 4a* are the experimental slip traces measured from the post-deformed pillars and the solid black lines are the theoretically calculated slip traces for the tested two crystal orientations (*Table 1*). For the near-[100] pillar (*Figure 3a, b*), the blue experimental slip traces show a good overlay with the calculated traces for slip system #8 (110)[$\bar{1}11$]/2 with deviation angles of 4 and 2° on surface 1 & 3 and surface 2 & 4 respectively (*Figure 3a*). The red experimental traces have good matches with the calculated trace for slip system #10 ($\bar{1}10$)[$\bar{1}\bar{1}1$]/2 with deviation angles of 3 and 6° on surface 1 & 3 and surface 2 & 4 respectively (*Figure 3b*). Meanwhile, the m_W values of slip system #8 and #10 are the highest two among all slip systems (*Figure 3b*). So, for HP Sn sample with a near-[100] orientation, two $\langle \bar{1}11 \rangle$ slip systems on the (110) plane are expected to activate. For the near-[001] pillar (*Figure 4a, b*), slip system #2 (010)[001] and #3 (110)[001] are highlighted because of their relatively large m_W values and high ranking among the 32 slip systems. It is found that the blue experimental slip trace has relatively small deviation angles to slip system #3 (*Figure 4a*), while the red slip traces show a good match with slip system #2 (*Figure 4b*). Although the slip systems #23 (011)[01 $\bar{1}$], #26 ($\bar{1}\bar{2}1$)[$\bar{1}01$], #21 (101)[10 $\bar{1}$] and #30 ($\bar{2}11$)[0 $\bar{1}1$] have higher values of m_W , they are unlikely to be active because their calculated slip planes do not match the measured slip traces in experiment and they have low rank in the likelihood of activity of common Sn slip systems according to ref^[23, 40]. Therefore, [001] direction slip on both (010) and (110) planes are expected to activate for

HP Sn with near-[001] orientation. The calculated slip traces are determined by considering all 32 slip systems of Sn for both near-[100] and near-[001] orientations.

In our case, σ_f about 40 MPa on average has been observed by testing these small and unconstrained geometries within a single crystal orientation, the initial σ_y has been used to extract the τ_{CRSS} to achieve activation of limited number of slip systems, rather than using the flow stress for activation of multiple slip systems in a multi-crystal sample (Philippi et al. ^[37]).

Our analysis in *Figure 2* shows that there is significant strain hardening before 2% of strain. Philippi et al. ^[37] measure flow stress and do not comment directly on strain hardening in their tests, but their stress-strain curves for their micropillar compression tests demonstrably show similar strain hardening to our results.

Furthermore, in the work of Philippi et al. ^[37] they report a size effect for the flow stress, which could be related both due to micro-pillar based size effects and strain hardening during testing. In our work, we have selected larger pillars (5 μm) and measured the CRSS to aim to measure properties that are useful for understanding bulk samples^[37], but size effect may exist. In this context, it is reassuring that our obtained τ_{CRSS} values and CRSS ratios match the macroscopic results ^[23] reasonably.

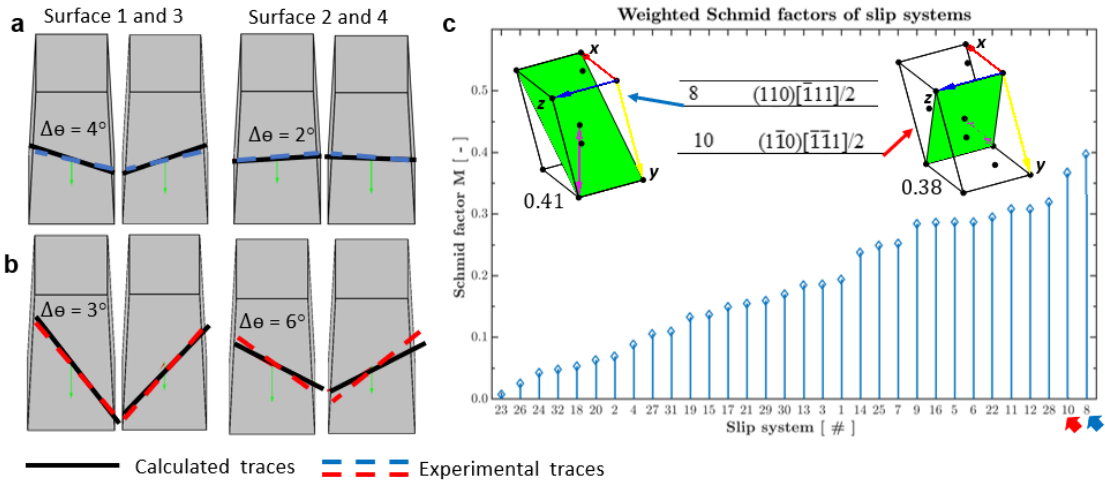


Figure 3. Analysis of the activated Sn slip systems for micropillar in near-[100] grain. (a, b) Models showing the mismatch between the experimentally measured slip traces and theoretically calculated slip traces. (c) The weighted Schmid factor (m_W) distribution vs. the slip system ranked according to their likelihood of activity with unit cells of the highest two m_W illustrated for the measured slip traces. The green shaded planes are the slip planes and the magenta arrows are the slip directions.

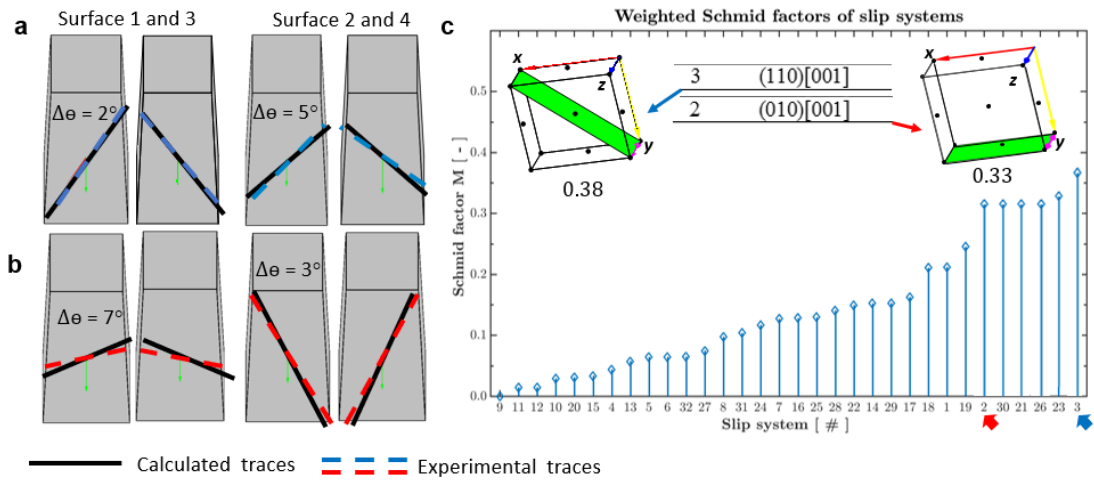


Figure 4. Analysis of the activated Sn slip systems for micropillar in near-[001] grain. (a, b) Models showing the mismatch between the experimentally measured slip traces and theoretically calculated slip traces. (c) The weighted Schmid factor (m_W) distribution vs. the slip system ranked according to their likelihood of activity with unit cells of the highest two m_W illustrated for the measured slip traces. The green shaded planes are the slip planes and the magenta arrows are the slip directions.

Uniaxial compression tests were carried out on single crystal high purity Sn micropillars with near-[100] and near-[001] orientations in the loading direction at room temperature. The deformation behaviour of the pillars has showed a strong dependence on crystal orientation with significant initial strain hardening, changes in level of yield stress and flow stress and stress drops have been observed during compression. Activation of two slip systems has been confirmed for the two tested pillars. The near-[100] pillar required higher applied stress than the near-[001] pillar to initiate the motion of dislocations. For the pillar with a near-[100] orientation in loading direction, two centripetal slips on (110) plane, i.e. slip systems $(110)[\bar{1}11]/2$ and $(1\bar{1}0)[\bar{1}\bar{1}1]/2$ were activated with $\tau_{CRSS}^{\{110\}\langle\bar{1}11\rangle/2} \sim 10.4 \pm 0.4$ MPa. For the pillar with a near-[001] orientation in loading direction, the [001] direction slip on both (010) and (110) planes, i.e. slip systems $(010)[001]$ and $(110)[001]$ were activated with $\tau_{CRSS}^{\{010\}\langle 001\rangle} \sim 3.9 \pm 0.3$ MPa. This work is a precursor study in directly measuring the values of τ_{CRSS} for the β -tin phase, as well as proving the validation of the ranking of the slip systems for tin^[40] and the estimation of the CRSS ratio from prior literature^[23]. Future work will be followed up to further measure the relative slip strengths of the β -tin system from single slip orientations to provide inputs into phenomenological crystal plasticity models.

TG drafted the initial manuscript and conducted the experimental work. FG and TBB supervised the work equally. All authors contributed to the final manuscript.

Data from this manuscript is available at: <link to be included upon final acceptance>.

We would like to thank EPSRC (EP/R018863/1) for funding this work. We would like to acknowledge Dr Siyang Wang for support in training of the Alemnis and NanoBuilder for the fabrication and compression of micropillars. We also very thankful to Prof Fionn Dunne, Dr Yilun Xu and Prof Christopher Gourlay and Dr Jingwei Xian for discussion in developing the Matlab code of Sn slip systems and experimental work. The microscope and loading frame used to conduct these experiments was supported through funding from Shell Global Solutions and is provided as part of the Harvey Flower EM suite at Imperial.

Reference

1. R.J. Coyle, K. Sweatman, and B. Arfaei, *JOM*, 67, 2394; (2015).
2. H. Ma and J.C. Suhling, *J. Mater. Sci.*, 44, 1141; (2009).
3. S. Cheng, Huang, C-M. and Pecht, M., *Microelectronics Reliab.*, 75, 77; (2017).
4. J.A. Depiver, S. Mallik, and E.H. Amalu, *J. Electron. Mater.*, 1; (2020).
5. H. Black, *Environ. Health Perspect.*, 113, 683; (2005).
6. J.W. Xian, G. Zeng, S.A. Belyakov, Q. Gu, K. Nogita, and C.M. Gourlay, *Intermetallics*, 91, 50; (2017).
7. E. S. Hedges, *Tin and its alloys: by Ernest S. Hedges*: Arnold, (1960).
8. T.R Bieler, H. Jiang, L.P. Lehman, T. Kirkpatrick, E.J. Cotts, and B. Nandagopal, *IEEE Trans. Compon. & Pack. Tech.*, 31, 370; (2008).
9. T.R. Bieler, B. Zhou, L. Blair, A. Zamiri, Amir, P. Darbandi, F. Pourboghrat, Y-K, Lee, and K-C. Liu, *J. Electron. Mater.*, 41, 283; (2012).

10. A.U. Telang T.R. Bieler, *J. Electron. Mater.*, 38, 2694; (2009).
11. Q. Zhou B. Zhou, T.R. Bieler, T.K. Lee, *J. Electron. Mater.*, 44, 895; (2015).
12. T. Gu, Y. Xu, C.M. Gourlay, T.B. and Britton, *Scripta Mater.*, 175, 55; (2020).
13. S. Mahin-Shirazi, B. Arfaei, S. Joshi, M. Anselm, P. Borgesen, E. Cotts, J. Wilcox and R. Coyle; Editor; 976; (2013).
14. J. K. Kivilahti T.T. Mattila, *Trans. Compon. & Pack. Tech.*, 33, (2010).
15. J. Han, S. Tan, and F. Guo, *J. Electron. Mater.*, 45, 6086; (2016).
16. K.E. Yazzie, J.J. Williams, and N. Chawla, *J. Electron. Mater.*, 41, 2519; (2012).
17. P.T. Vianco, J.A. Rejent, and A.C. Kilgo, *J. Electron. Mater.*, 33, 1473; (2004).
18. Q. K. Zhang and Z.F. Zhang, *Acta Mater.*, 59, 6017; (2011).
19. M. A. Matin, W.P. Vellinga, and M.G.D. Geers, M. G. D., *Mater. Sci. & Engineer.: A*, 431, 166; (2006).
20. T. Gu, C.M. Gourlay, and T.B. Britton, *J. Electron. Mater.*, 48, 107; (2019).
21. T. Gu, V.S. Tong, C.M. Gourlay, and T.B. Britton, *Acta Mater.*, 196, 31; (2020).
22. W.P. Vellinga M.A. Matin, M.G.D. Geers, , *Mater. Sci. & Engineer.: A*, 445, 73; (2007).
23. A. Zamiri, T.B. Bieler, and F. Pourboghra, *J. Electron. Mater.*, 38, 231; (2009).
24. B. Zhou, T.B. Bieler, T.K. Lee, and K.C. Liu, *J. Electron. Mater.*, 38, 2702; (2009).
25. Y. Zuo, T.B. Bieler, Q. Zhou, L. Ma, and F. Guo, *J. Electron. Mater.*, 47, 1881; (2018).
26. C.R. Mayer, Lotfian, S., Molina-Aldareguia, J. and Chawla, N., *Advanced Engineering Materials*, 17, 1168; (2015).
27. M.D. Uchic, D.M. Dimiduk, J.N. Florando, and W.D. Nix, *Sci.*, 305, 986; (2004)..
28. H. Bei, S. Shim, G.M. Pharr, and E.P. George, *Acta Mater.*, 56, 4762; (2008).
29. G. Guillonneau, M. Mieszala, J. Wehrs, J. Schwiedrzik, S. Grop, D. Frey, L. Philippe, J-M. Breguet, J. Michler, and J.M. Wheeler, *Mater. & Des.*, 148, 39; (2018).
30. T.E.J. Edwards, F.D. Gioacchino, R. Muñoz-Moreno, and W.J. Clegg, *Scripta Mater.*, 118, 46; (2016).
31. Z. Zhang, T-S. Jun, T.B. Britton, F.P.E. and Dunne, *Acta Mater.*, 118, 317; (2016).
32. J.Y. Wu, Y.S. Chiu, Y.W. Wang, and C.R. Kao, *Mater. Sci. & Engineer.: A*, 753, 22; (2019).
33. L. Jiang and N. Chawla, *Scripta Mater.*, 63, 480; (2010).
34. S. Wang, F. Giuliani, and T.B. Britton, *Scripta Mater.*, 162, 451; (2019).
35. J.T. Pürstl, H.O. Jones, T.E.J. Edwards, R.P. Thompson, F.D. Gioacchino,, N.G. Jones, and W.J. Clegg, *Mater. Sci. & Engineer.: A*, 800, 140323; (2020).
36. J.Y. Wu, Y.S. Chiu, Y.W. Wang, and C.R. Kao, *Mater. Sci. & Engineer.: A*, 753, 22; (2019).
37. B. Philippi, C. Kirchlechner, J.S. Micha, and G. Dehm, *Acta Mater.*, 115, 76; (2016).

38. C.S. Kaira, S.S. Singh, A. Kirubanandham, and N. Chawla, *Acta Mater.*, 120, 56; (2016).
39. J. Gong and A.J. Wilkinson, *Scripta Mater.*, 114, 17; (2016).
40. M. Fujiwara and T. Hirokawa, *J. Jpn. Inst. Met.*, 51, 830; (1987).
41. K. W. Moon, W.J. Boettinger, U.R. Kattner, F.S. Biancaniello, and C.A. Handwerker, *J. Electron. Mater.*, 29, 1122; (2000).

Supplementary Material:

Family	Slip system	CRSS ratio	CRSS ratio*
1	1 (100)[001]	1	1.46
	2 (010)[001]	1	1.46
2	3 (110)[001]	1	1
	4 ($\bar{1}\bar{1}0$)[001]	1	1
3	5 (100)[010]	1.05	2.54
	6 (010)[100]	1.05	2.54
4	7 (110)[$\bar{1}\bar{1}1$]/2	1.1	1.77
	8 (110)[$\bar{1}11$]/2	1.1	1.77
	9 ($\bar{1}\bar{1}0$)[111]/2	1.1	1.77
	10 ($\bar{1}\bar{1}0$)[$\bar{1}\bar{1}1$]/2	1.1	1.77
5	11 (110)[$\bar{1}\bar{1}0$]	1.2	-
	12 ($\bar{1}\bar{1}0$)[110]	1.2	-
6	13 (010)[101]	1.25	2.92
	14 (010)[$10\bar{1}$]	1.25	2.92
	15 (100)[011]	1.25	2.92
	16 (100)[$01\bar{1}$]	1.25	2.92
7	17 (001)[100]	1.3	-
	18 (001)[010]	1.3	-
8	19 (001)[110]	1.4	-
	20 (001)[$\bar{1}\bar{1}0$]	1.4	-
9	21 (101)[$10\bar{1}$]	1.5	1.23
	22 ($10\bar{1}$)[101]	1.5	1.23
	23 (011)[$01\bar{1}$]	1.5	1.23
	24 ($01\bar{1}$)[011]	1.5	1.23
10	25 (121)[$\bar{1}01$]	1.5	1.15
	26 ($\bar{1}\bar{2}1$)[$\bar{1}01$]	1.5	1.15
	27 ($\bar{1}21$)[101]	1.5	1.15
	28 ($\bar{1}\bar{2}1$)[101]	1.5	1.15
	29 (211)[$0\bar{1}1$]	1.5	1.15
	30 ($\bar{2}11$)[$0\bar{1}1$]	1.5	1.15
	31 ($2\bar{1}1$)[011]	1.5	1.15
	32 ($2\bar{1}1$)[011]	1.5	1.15

Table S1. The common Sn slip systems ^[1] with CRSS (the critical resolved shear stress) ratios given. The values of CRSS ratio are estimated from by Zamiri et al. ^[2] and the values of CRSS ratio* are from Matin et al. ^[3].

Pillar	Yield Stress σ_y (MPa)		Flow Stress σ_f (MPa)	
	[100]	[001]	[100]	[001]
1	27.8	11.4	72.9	35.0
2	22.7	12.3	56.1	33.0
3	35.7	12.9	45.5	36.5
4	28.9	10.5	49.3	34.2
5	9.9	10.2	17.5	32.7
6	-	9.6	-	28.9
7	-	8.9	-	12.6

Table S3. *The values of yield stress and flow stress for all tested pillars.*

1. M. Fujiwara and T. Hirokawa, J Jpn Inst Met, 1987, **51**(9): p. 830.
2. A. Zamiri, T.R. Bieler and F. Pourboghra, J Electron Mater, 2009, **38**(2): p. 231.
3. M. A. Matin, W.P. Vellinga and M.G.D. Geers, Mater Sci & Engineer: A, 2006, **431**(1-2): p. 166.